Advanced Functional Materials

ADVANCED FUNCTIONAL MATERIALS
www.afm-journal.de

RESEARCH ARTICLE OPEN ACCESS

A Bilayered Inorganic-Metal Interface Enables Highly Reversible Aluminum Deposition for Long-Life Aqueous Batteries

Shuang Cheng[1,2] | Xiaomin Cheng[2,3] | Linge Li[1,2] | Yaping Wang[4] | Jing Zhang[5] | Yongzheng Zhang[6] | Hongzhen Lin[1,2] | Jian Wang[2,7,8]

[1]School of Nano-Technology and Nano-Bionics, University of Science and Technology of China, Hefei, China | [2]i-Lab, Suzhou Institute of Nano-Tech and Nano-Bionics, Chinese Academy of Sciences, Suzhou, China | [3]Guangdong Institute of Semiconductor Micro-Nano Manufacturing Technology, Guangdong, China | [4]School of Electrical and Information Engineering, Tongling University, Tongling, China | [5]School of Materials Science and Engineering, Xi'an University of Technology, Xi'an, China | [6]School of Textile & Clothing, Nantong University, Nantong, China | [7]Helmholtz Institute Ulm (HIU), Ulm, Germany | [8]Karlsruhe Institute of Technology (KIT), Karlsruhe, Germany

Correspondence: Xiaomin Cheng (xmcheng2023@sinano.ac.cn) | Hongzhen Lin (hzlin2010@sinano.ac.cn) | Jian Wang (jian.wang@kit.edu; wangjian2014@sinano.ac.cn)

Received: 22 January 2026 | **Revised:** 3 April 2026 | **Accepted:** 16 May 2026

Keywords: aqueous aluminum metal batteries | gradient Sn/SnO$_x$ synergistic interfacial layer | hydrogen evolution suppression | interfacial kinetics enhanced

ABSTRACT

Rechargeable aqueous aluminum metal batteries (AAMBs) represent a promising large-scale energy storage technology due to their unique advantages of high volumetric energy density, low cost, and operational safety. However, their cyclic stability and Coulombic efficiency are constrained by the sluggish interfacial kinetics originating from the stable $[Al(H_2O)_6]^{3+}$ complex, which leads to rigorous issues such as hydrogen evolution reaction and surface passivation. Herein, a gradient Sn/SnO$_x$ synergistic interfacial layer with high aluminophilicity and ion-buffering capability (termed as HAIBSL) was integrated on metallic Al anode by one-step chemical displacement reaction, applicable also to Cu/CuO$_x$ and Cd/CdO$_x$ interphases. As a prototype, Sn/SnO$_x$ layer not only accelerates Al^{3+} desolvation kinetics and uniform plating, but also acts as a barrier to avoid water-induced side reactions, as confirmed by electrochemical and theoretical experiments. Moreover, X-ray diffraction (XRD) and time-of-flight secondary ion mass spectrometry (TOF-SIMS) confirm the excellent cycling stability of this layer. Consequently, the symmetrical HAIBSL@Al cell demonstrates ultrastable cycling with a low overpotential for 1800 h at 0.05 mA cm^{-2}. Moreover, the HAIBSL@Al can be compatible with multiple cathodes and exhibits a cycling life of 700 cycles with potassium cobalt hexacyanoferrate (II) cathode, underscoring the gradient synergistic interfacial layer as a robust and versatile strategy for AAMBs.

1 | Introduction

Rechargeable aqueous aluminum metal batteries (AAMBs) represent an attractive candidate for next-generation energy storage, owing to the high theoretical capacities (8056 mAh cm^{-3} and 2980 mAh g^{-1}) enabled by three-electron transfer, as well as the abundance and low cost of aluminum [1–4]. Nevertheless, the practical application of AAMBs faces considerable challenges, primarily stemming from the hydrogen evolution reaction (HER) and the formation of passivating $Al(OH)_3$ layers [5–8]. These parasitic side reactions severely impair Coulombic efficiency (CE) and cycling stability. The fundamental obstacle stems from the exceptionally stable solvation structure of Al^{3+} in the aqueous electrolyte, specifically the $[Al(H_2O)_6]^{3+}$ complex, which exhibits

---

a remarkably high hydration energy of approximately −4525 kJ mol^{-1} [9, 10]. Such a robust solvation structure leads to sluggish interfacial desolvation kinetics, imposing a substantial energy barrier that impedes efficient charge transfer and reversible Al deposition [11–13].

To address this fundamental challenge, considerable research efforts have been devoted to tailoring the solvation structure of the $[Al(H_2O)_6]^{3+}$. Traditional electrolyte engineering strategies, which involve the use of high-concentration salts [14–17], organic additives [18–22], or alternative aluminum salts such as $Al(OTf)_3$, are designed to weaken the primary solvation shell [23]. Although partially effective, these bulk electrolyte modifications typically introduce undesirable trade-offs, including reduced ionic conductivity, increased viscosity, higher cost, and persistent corrosion issues [24–26]. As a result, a clear paradigm shift has occurred in the field, with research focus moving from global electrolyte optimization toward the precise engineering of the local electrode/electrolyte interface [5, 6, 27, 28]. Encouragingly, constructing an artificial electrode interface (AEI) is widely regarded as a more targeted and promising approach to directly control interfacial processes [29–34]. An ideal AEI should simultaneously fulfill the following critical functions: (i) facilitates rapid Al^{3+} desolvation; (ii) homogenizes lateral Al^{3+} flux to prevent dendrite formation; (iii) provides sufficient mechanical robustness against plating/stripping stresses; and (iv) maintains persistent electrochemical and structural integrity.

Currently developed strategies for constructing such AEIs can be broadly categorized into several types. One approach involves ex-situ pretreatment using ionic liquids or deep eutectic solvents to form hybrid organic-inorganic solid electrolyte interphases [35, 36]. A second strategy employs in situ techniques to generate inorganic protective layers, such as those based on Mn/Ti/Zr compounds [5] or AlF_3 [37]. A third route utilizes polymer coatings [27, 38], for example, polyvinylidene fluoride [6], to physically block water ingress and guide uniform Al^{3+} deposition. Despite these advances, prevailing strategies are frequently limited in key aspects. Many lack synergistic multifunctionality and therefore fail to concurrently and effectively address the intertwined requirements of rapid desolvation, homogeneous ion flux, and mechanical durability. Moreover, existing fabrication processes are often complex, energy-intensive or difficult to scale, which significantly hinders their practical implementation [27, 39–41].

Hence, the highly aluminophilic and ion-buffering synergistic Al anodes containing metallic M phase and MO_x phase (M = Sn, Cu, Cd) at the nanoscale are well-designed and fabricated via in situ one-step chemical displacement reaction to accelerate the $[Al(H_2O)_6]^{3+}$ desolvation and alleviate side reactions. With electron microscopy, Raman spectroscopy, and theoretical simulations proven, the prototype Sn/SnO_x engineered on the Al anode (denoted as HAIBSL@Al) capitalizes on the distinct yet complementary properties of its two constituents. The metallic Sn domains offer strong aluminophilic adsorption sites that preferentially interact with Al^{3+} and substantially reduce the energy barrier for desolvation, while the SnO_x matrix functions as an ion-conductive buffer that guides and homogenizes lateral Al^{3+} transport across the electrode surface, suppressing localized deposition and dendrite growth. The inherently compact HAIBSL serves as an efficient physical barrier, effectively inhibiting water permeation toward the Al interface and consequently suppressing HER and passivation. Furthermore, its structural integrity during cycling is corroborated by the ex-situ XRD and TOF-SIMS. Consequently, the HAIBSL@Al symmetric cell exhibited exceptional stability with a low overpotential of approximately 500 mV for over 1800 h at 0.05 mA cm^{-2}. When paired with various cathode materials such as potassium cobalt hexacyanoferrate (II) and α-MnO_2 using a low-cost and environmentally benign 0.5 M $Al_2(SO_4)_3$ electrolyte, the HAIBSL@Al anode enabled significantly reduced polarization, high specific capacity, superior cycling stability, and excellent rate capability, substantially outperforming bare Al anode. This work presents a scalable materials and fabrication paradigm for developing stable metal anodes in AAMBs, offering a generalizable pathway for future research.

2 | Results and Discussion

As proof, Al foils modified with a conformal Sn/SnO_x composite layer were successfully synthesized via one-step chemical displacement reaction, as shown in Figure 1A. Specifically, the immersion of an Al sheet into an anhydrous ethanol solution of $SnCl_4{\cdot}5H_2O$ initiates a coupled redox-hydrolysis process. Trace water induces partial hydrolysis of Sn^{4+}, generating SnO_x and releasing H^+. The resulting acidic environment then dissolves the native Al_2O_3 layer, exposing fresh Al that subsequently reduces Sn^{4+} to metallic Sn via displacement, thereby forming the composite Sn/SnO_x layer. This synergistic layer provides dual functionality: high Al affinity (from Sn) [38, 39] and ion-buffering capacity (from SnO_x) [42]. Compared to the bare Al anode (Figure S1), the XRD pattern of the HAIBSL@Al anode (Figure 1B) shows a prominent and dominant peak corresponding to the (101) crystal plane of Sn, except for the characteristic peaks of metallic Al [43]. Notably, the pattern shows no detectable signals from impurity phases or SnO_x. The XRD patterns confirm that crystalline metallic Sn is successfully formed and integrated into the composite structure, whereas any SnO_x present is confined to an amorphous phase. Scanning electron microscopy (SEM) was employed to examine the surface morphology and structure of the Al anode before and after treatment. After the displacement process, the HAIBSL forms throughout the Al substrate surface (Figure 1C), which presents a sharp contrast to the surface of bare Al (Figure S2). Energy dispersive X-ray spectroscopy (EDS) analysis (Figures S3 and S4) confirmed the homogeneous distribution of Al, O, Sn elements across the HAIBSL@Al electrode surface. Furthermore, the cross-sectional SEM image ascertains the obvious boundary between the Al substrate and HAIBSL (Figure 1D), where the Al, O, and Sn elements are evenly distributed across the HAIBSL@Al electrode (Figure S5). Under the same fabrication conditions, the copper/copper oxide (denoted as Cu/CuO_x@Al) and cadmium/cadmium oxide (denoted as Cd/CdO_x@Al) exhibit morphologies comparable to that of HAIBSL (Figures S6–S8), demonstrating the versatility of the preparation method. As shown in Figure 1E, the contact angle on the HAIBSL@Al electrode (19°) is much smaller than that of the bare Al (58.96°), indicating the remarkably improved surface wettability of the HAIBSL@Al electrode enabled by its electrolyte-philicity and high aluminophilicity [44, 45]. X-ray photoelectron spectroscopy (XPS) survey spectrum attests to the presence of Al, Sn, and O

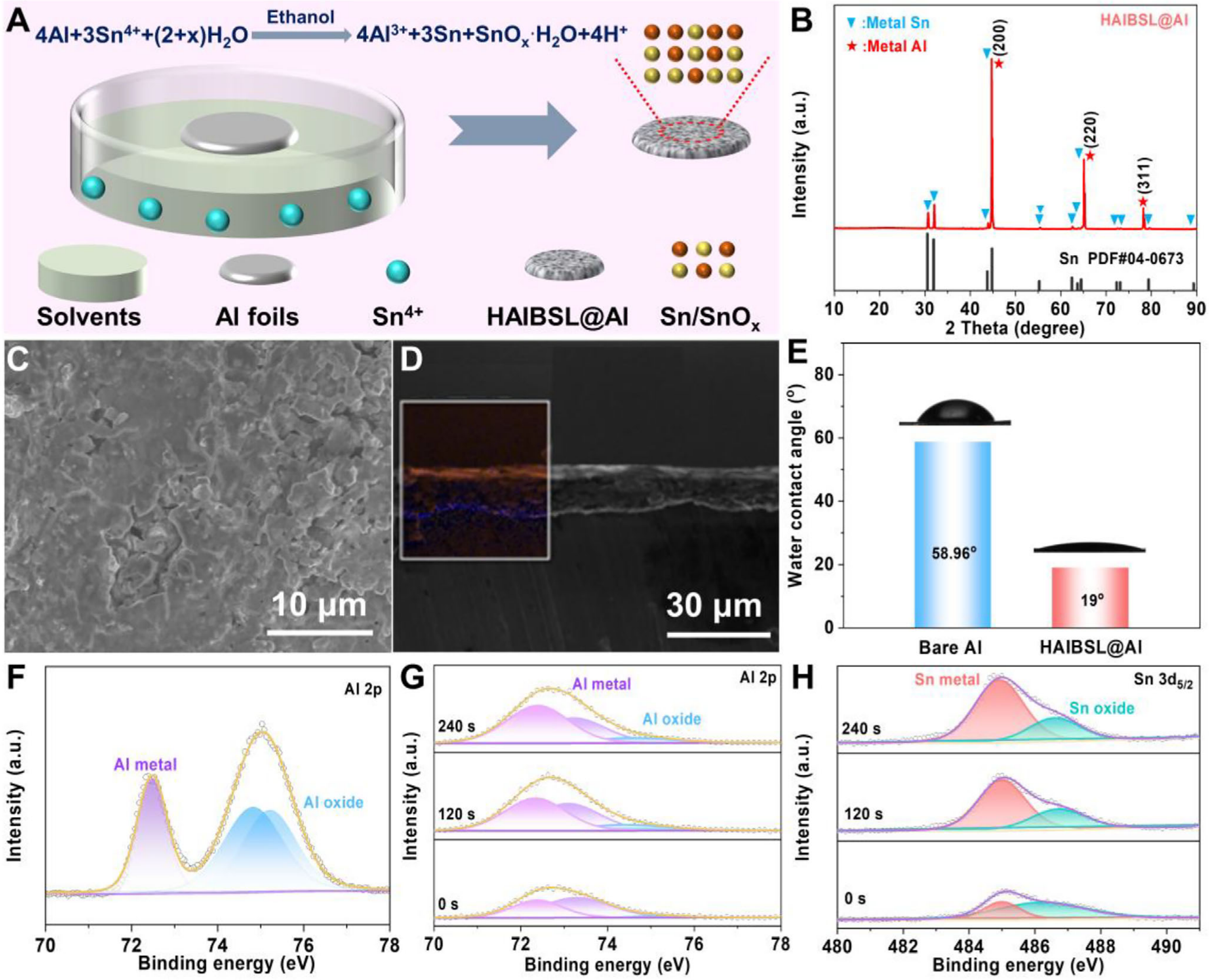

FIGURE 1 | (A) Schematic illustration of the modification process of the HAIBSL@Al electrode. (B) XRD pattern and (C) Top-view SEM image of the HAIBSL@Al electrode. (D) Cross-sectional SEM image of the HAIBSL@Al electrode. (E) Comparison of contact angles of the electrolyte on the surface of bare Al and HAIBSL@Al. (F) Al 2p spectra of bare Al. XPS spectra of (G) Al 2p and (H) Sn 3d on HAIBSL@Al after Ar^+ sputtering for 0 to 4 min.

elements in the as-prepared HAIBSL@Al. The Al 2p spectrum of bare Al (Figure 1F) reveals the presence of peaks corresponding to metallic Al^0 and oxidized Al^{3+} [27]. To probe the spatial distribution of SnO_x and metallic Sn in the HAIBSL architecture, in-depth XPS was performed. As shown in Figure 1G, the Al 2p spectrum before sputtering is dominated by the metallic Al peak at 72.48 eV, with a faint contribution from Al oxide at 75.03 eV. With progressive sputtering, the spectral response continues to be dominated by metallic Al, whereas signals corresponding to aluminum oxide remain negligible throughout the depth profile. These results unambiguously demonstrate that the engineered HAIBSL effectively suppresses oxidative formation on the Al anode surface. Encouragingly, the Sn 3d spectrum of HAIBSL@Al prior to sputtering exhibits peaks corresponding to metallic Sn and SnO_x with comparable intensities [39]. As the sputtering depth increases, the ratio of metallic Sn to SnO_x progressively rises, clearly revealing a gradient distribution of Sn/SnO_x composite within the HAIBSL (Figure 1H), showing a similar gradient distribution to that in our previous report [46]. The above results confirm the successful fabrication of the HAIBSL on the Al surface.

To evaluate the feasibility of Al deposition on HAIBSL@Al versus bare Al electrodes, density functional theory (DFT) was adopted to calculate the adsorption energy of Al atoms on the respective substrates. As shown in Figure S9, the adsorption energies of a single Al atom on Al (200), Sn (101), Sn (200), and SnO_2 (110) surfaces were compared. The calculated adsorption energy for Al on Sn (101) surface is −2.43 eV, which is significantly more negative than Al atom on Al (200) surface (−0.64 eV) (Figure 2A). The stronger adsorption between the Al atom and the HAIBSL can effectively boost the desolvation of hydrated Al ions [38]. Meanwhile, the SnO_x layer with the comparable adsorption capability serves as an ion-buffering layer via weak Al^{3+} adsorption, which homogenizes interfacial Al^{3+} flux, collectively stabilizing the electrode/electrolyte interface and improving the cycling reversibility. Linear sweep voltammetry (LSV) results (Figure 2B) show that HAIBSL@Al exhibits a lower

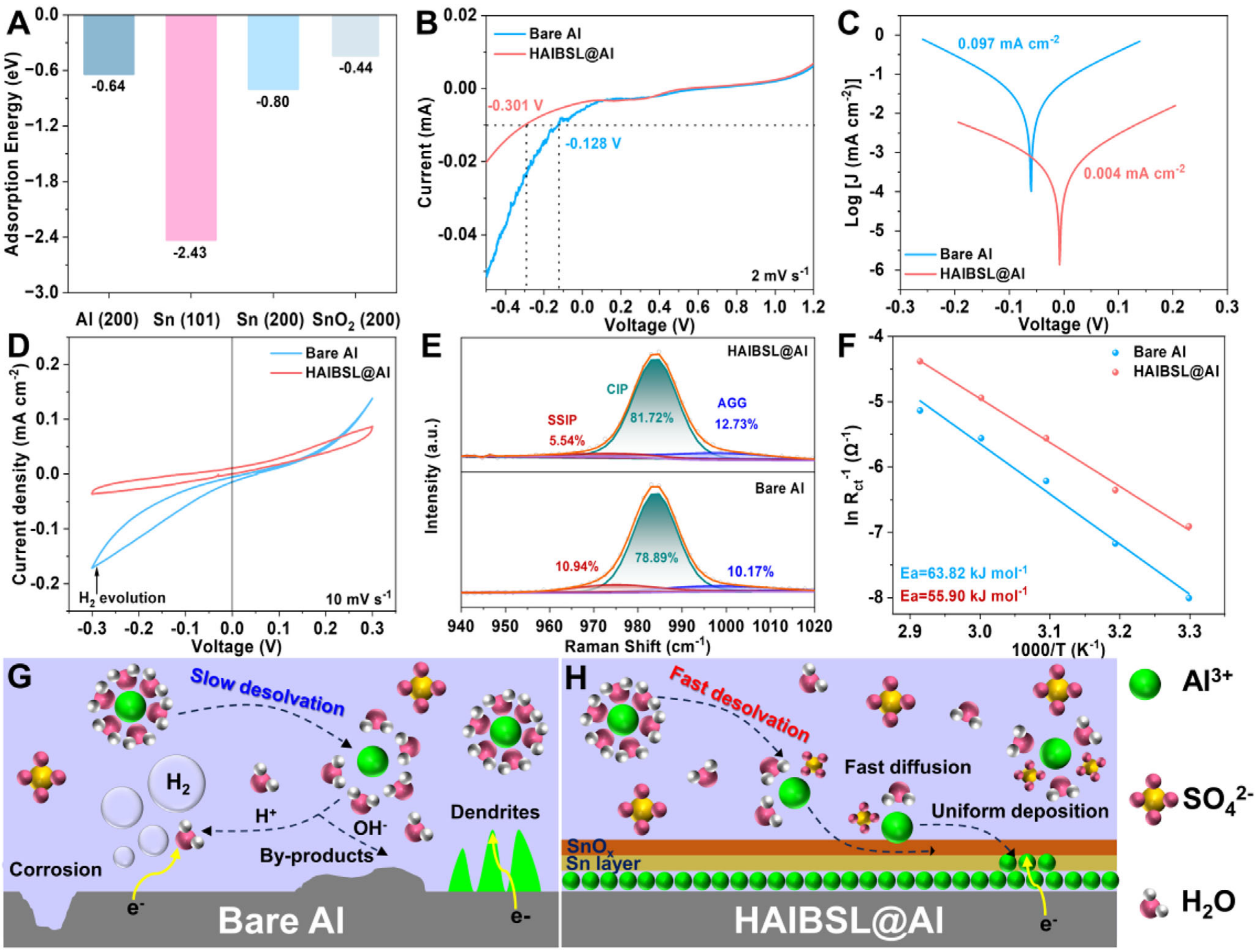

FIGURE 2 | (A) Comparison of the adsorption energy of Al on Al, Sn and SnO_2 substrates. (B) LSV curves and (C) Tafel curves of bare Al and HAIBSL@Al electrodes. (D) CV curves of symmetric cells using bare Al and HAIBSL@Al electrodes with a scan rate of 10 mV s^{-1}. (E) Raman spectra of the 0.5 M $Al_2(SO_4)_3$ electrolyte at the bare Al and HAIBSL@Al electrode interfaces. (F) Desolvation activation energy derived from the Arrhenius curves of bare Al and HAIBSL@Al electrodes. (G) HER and dendrite growth on the bare Al electrode. (H) Synergistic desolvation mechanism on HAIBSL@Al.

onset potential (-0.301 V) than bare Al (−0.128 V). This indicates a significantly suppressed HER on the HAIBSL@Al electrode, which can be attributed to faster desolvation kinetics [6]. To elucidate the origin of the suppressed HER and accelerated desolvation process, we performed theoretical calculations to investigate H_2O adsorption behaviors on bare Al and HAIBSL@Al surfaces. As shown in Figures S10 and S11, the H_2O adsorption energy on Sn (101) (−1.83 eV) is higher than that on Al (200) (−0.39 eV), and the high dissociation barrier on Sn suppresses HER while accelerating desolvation, validating the HAIBSL@Al interface design. To further validate the inhibition of HER, in situ optical microscopy and pH measurements were employed during the electroplating process at 0.2 mA cm^{-2}. As shown in Figure S12, the HAIBSL@Al electrode exhibits negligible bubble generation throughout the Al deposition process, whereas gas bubbles on the bare Al electrode progressively increase with time, confirming the effective inhibition of HER by HAIBSL. Meanwhile, compared with bare Al, the pH value of the HAIBSL@Al electrode remains more stable (Figure S13), providing additional evidence for its pronounced ability to suppress HER. Furthermore, the anticorrosion performance was assessed. Tafel analysis reveals a lower corrosion current density for the HAIBSL@Al symmetric cell (0.004 mA cm^{-2}) compared to that of bare Al (0.097 mA cm^{-2}), suggesting both a reduced tendency and a slower corrosion rate for HAIBSL@Al (Figure 2C) [27]. Cyclic voltammetry (CV) tests were conducted on HAIBSL@Al and Al symmetric cells to compare the behavior of HAIBSL@Al and Al electrodes (Figure 2D). The bare Al shows an asymmetric curve, with a typical HER-shaped peak on the plating side, reflecting inefficient Al plating and severe HER. On the stripping side (positive voltage), suppressed current density is observed, possibly due to the surface passivation layer. In contrast, the HAIBSL@Al electrode displays a more symmetric curve and enhanced current density, which can be attributed to the improved Al stripping/plating [38].

To further investigate the interactions between hydrated Al^{3+} and the HAIBSL, Raman spectroscopy was employed. As shown in Figure 2E, the evolution of the solvation structure is clearly observed, transitioning from solvent-separated ion pairs (SSIP) to contact ion pairs (CIP) and Aggregates (AGG). At the HAIBSL@Al/electrolyte interface, the proportion of CIP rises significantly to 81.72% compared with 78.89% at the bare Al/electrolyte interface, and the AGG proportion increases to

12.73% compared with 10.17% at the bare Al/electrolyte interface. These results demonstrate that the presence of HAIBSL substantially enhances the coupling between Al^{3+} and SO_4^{2-} [9, 13]. To quantitatively elucidate the desolvation kinetics of hydrated Al^{3+} and the concomitant Al^{3+} transport behavior, the activation energy (E_a) was derived from the Arrhenius equation (Figure 2F and Figure S14). The HAIBSL@Al electrode exhibits a substantially lower E_a of 55.90 kJ mol^{-1} relative to that of the bare Al electrode (63.82 kJ mol^{-1}). This pronounced reduction in E_a signifies diminished energy barriers for the desolvation process, which not only promotes a more efficient release of free Al^{3+} but also facilitates subsequent Al^{3+} migration within the HAIBSL interphase [23]. In comparison with severe side reactions such as HER and dendritic growth observed on bare Al (Figure 2G), the designed HAIBSL effectively suppresses these issues. As illustrated in Figure 2H, the metallic Sn layer effectively reduces the desolvation energy barrier of hydrated Al^{3+} due to its high Al affinity, while the SnO_x ion-buffering layer promotes lateral diffusion of Al^{3+}. This synergy regulates the Al^{3+} transport kinetics, thereby inhibiting dendrite growth and enabling homogeneous Al deposition [47].

To evaluate the influence of the HAIBSL on electrochemical performance, symmetric cells were fabricated using bare Al and HAIBSL@Al electrodes. Electrolyte concentration is known to significantly affect the stripping/plating behavior of metal electrodes [27]. Optical images in Figure S15A indicate that aluminum sulfate octadecahydrate ($Al_2(SO_4)_3{\cdot}18H_2O$) exhibits a solubility of up to 1.0 M in deionized water. Comparative LSV results indicate that the optimized 0.5 M $Al_2(SO_4)_3$ electrolyte is the most stable among those tested (Figure S15B). Moreover, these measurements confirm that it enables symmetric cells to operate with both low overpotential and high stability (Figure S16). As known, the thickness can affect the ion/atom diffusion and distribution [48]. By adjusting the reaction time, HAIBSL@Al electrodes with different thicknesses from 1 to 6 µm were obtained. The cross-sectional SEM images and EDS mappings of Figure S17 show all elements are well distributed in the HAIBSL@Al. Among them, the optimal HAIBSL@Al (3.5 µm, Figure S5) delivers the most stable cycling and longest lifespan, which is much better than the others, indicating the best thickness is ≈3.5 µm. Electrochemical impedance spectroscopy (EIS) was performed on symmetric cells to further elucidate the enhanced Al^{3+} transport properties (Figure 3A). The charge-transfer resistance of the bare Al symmetric cell is approximately 2.5 times higher than that of the HAIBSL@Al cell, highlighting the critical role of the HAIBSL in promoting charge-transfer kinetics. Furthermore, the HAIBSL@Al symmetric cell exhibits excellent rate performance, as shown in Figure 3B and Figure S18. Specifically, as the current density increases from 0.05 to 0.2 mA cm^{-2}, voltage hysteresis values of 23, 120, and 300 mV are recorded, which are significantly lower than those observed for the symmetric cell with bare Al. The accelerated desolvation kinetics and enhanced Al^{3+} transport collectively optimize Al nucleation and growth behavior. As shown in Figure 3C, the HAIBSL@Al electrode exhibits a lower nucleation overpotential of only 50 mV, compared to 520 mV for bare Al. The improved desolvation kinetics and facilitated Al^{3+} diffusion are further verified in symmetric cells (Figure 3D). The HAIBSL@Al cell demonstrates outstanding long-term stability, operating for over 1800 h with overpotentials of approximately 500 mV at 0.05 mA cm^{-2}, whereas the bare Al cell sustains less than 600 h and shows significant voltage fluctuation due to sluggish desolvation kinetics. Moreover, when cycled at 0.1 mA cm^{-2} with a capacity of 0.1 mAh cm^{-2}, the HAIBSL@Al cell maintains a low voltage hysteresis of approximately 330 mV for 100 h (Figure S16B). When tested under elevated current densities or areal capacities (0.2 mA cm^{-2} for 0.2 mAh cm^{-2} and 0.05 mA cm^{-2} for 0.5 mAh cm^{-2}), the HAIBSL@Al cell maintains low voltage hysteresis of 500 mV for 100 h, and 550 mV for over 300 h, respectively (Figure 3E and Figure S19). Notably, as shown in Figure S20, the cell operates stably even under an ultrahigh areal capacity of 1 mAh cm^{-2} at 0.1 mA cm^{-2}, further confirming that the HAIBSL effectively lowers the desolvation energy barrier and thereby facilitates Al^{3+} diffusion kinetics. Compared with previously reported AAMBs, the cycling performance of HAIBSL@Al represents a notable advancement, as comprehensively summarized in Figure 3F. To demonstrate the general applicability of this approach, both Cu/CuO_x@Al and Cd/CdO_x@Al anodes also demonstrate stable cycling over 100 h at 0.1 mA cm^{-2} with a capacity of 0.1 mAh cm^{-2} (Figure 3G), highlighting the broad applicability of the proposed fabrication method for diverse interfacial designs.

The morphological evolution of Al deposition on HAIBSL@Al and bare Al electrode under a current density of 0.05 mA cm^{-2} was further investigated by ex-situ SEM. On the bare Al electrode, even at the early plating stage (0.1 mAh cm^{-2}, Figure 4A), small block-like Al protrusions and attack pits are observed. These protrusions intensify the tip effect, promote local Al^{3+} enrichment, and lead to inhomogeneous deposition, ultimately triggering dendrite growth. As the areal capacity increases to 0.2 mAh cm^{-2}, these protrusions grow larger and thicker, accompanied by the expanding corrosion pits induced by the HER (Figure 4B). At a capacity of 0.5 mAh cm^{-2}, numerous Al blocks and pits cover the entire electrode surface, resulting in a rough and non-uniform morphology (Figure 4C). Such uneven surface morphology can induce severe volume changes, highly polarized plating/stripping potentials during cycling, and even battery failure. In contrast, the HAIBSL@Al electrode exhibits a laterally interconnected Al-grain network at a low deposition capacity of 0.1 mAh cm^{-2} (Figure 4D). When the capacity is raised to 0.2 mAh cm^{-2}, Al deposits expand laterally across the electrode surface (Figure 4E). At a capacity of 0.5 mAh cm^{-2}, the laterally growing Al deposits coalesce into a relatively flat and compact layer (Figure 4F). Furthermore, exsitu XRD was conducted to investigate the crystal structure of the HAIBSL@Al electrodes at different plating capacities (Figure 4G). The Sn (101) diffraction peak remains visible even as the plating capacity increases, indicating that the HAIBSL maintains structure integrity on the Al surface. Concurrently, the appearance of characteristic Al diffraction peaks confirms successful Al deposition. Additionally, time-of-flight secondary ion mass spectrometry (TOF-SIMS) was employed to analyze the plating morphology of bare Al and HAIBSL@Al electrodes after cycling. In contrast to the rough and heterogeneous deposition observed on bare Al (Figure 4H), the HAIBSL@Al electrode exhibits a remarkably uniform and smooth surface (Figure 4I). Furthermore, the 3D overlay of SnO^- signals from the cycled HAIBSL@Al electrode (Figure S21) demonstrates a homogeneous distribution of Sn, further confirming the structural stability of the HAIBSL during cycling. After 30 cycles, SEM and EDS demonstrate excellent structural integrity and uniform elemental distribution of the HAIBSL (Figure S22), while XPS further

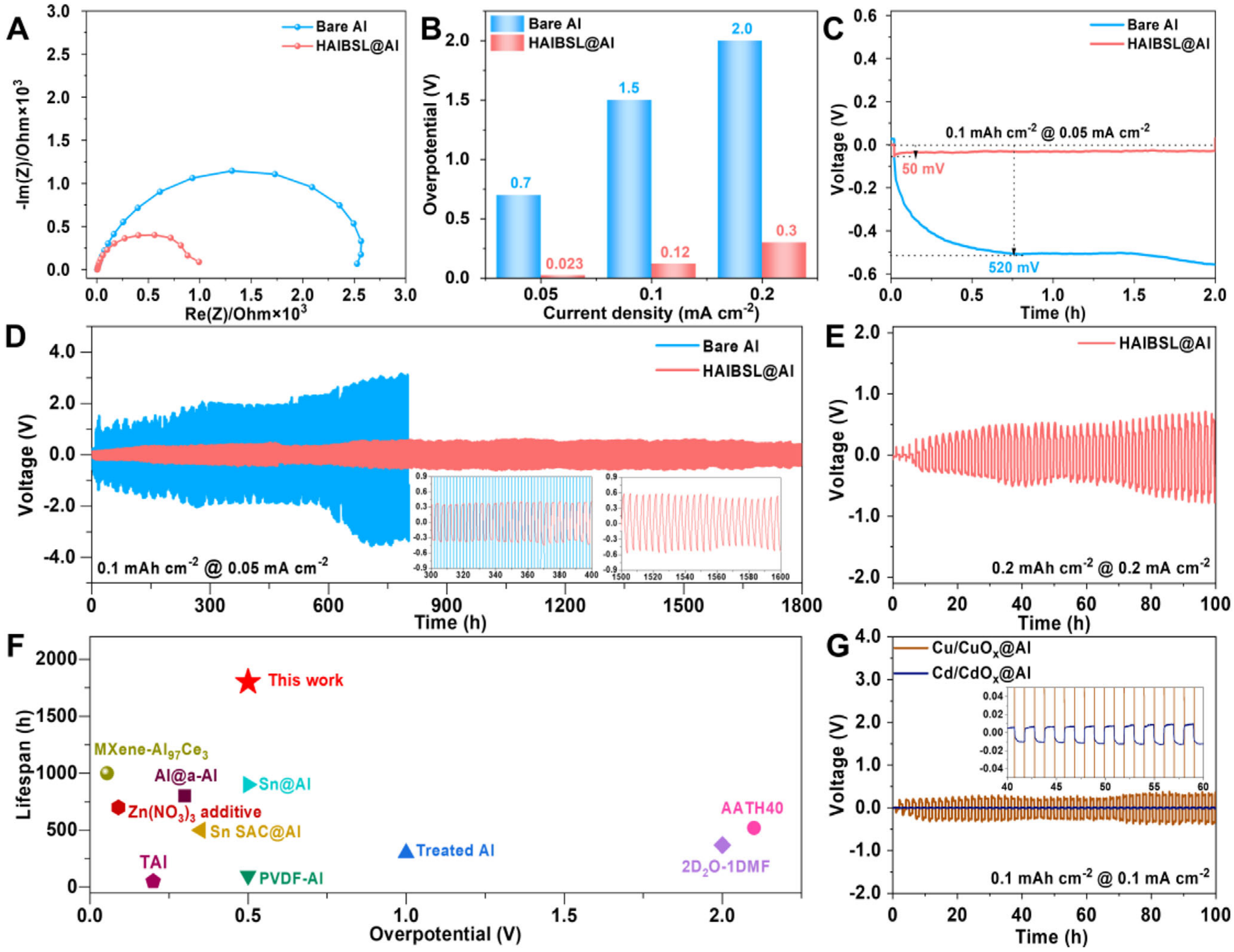

FIGURE 3 | (A) Nyquist plots, (B) comparison of overpotentials at different current densities, (C) comparison of initial nucleation barriers, and (D) long-term galvanostatic charge/discharge cycles of symmetric cell at 0.05 mA cm^{-2} for bare Al and HAIBSL@Al electrodes. (E) Voltage profiles of symmetric cells with HAIBSL@Al at a high current density of 0.2 mA cm^{-2} and a high areal capacity of 0.2 mAh cm^{-2}. (F) Comparison of plating overpotentials and cycle life between this work and reported works on AAMBs. (G) Voltage profiles of symmetric cells with Cu/CuO$_x$@Al and Cd/CdO$_x$@Al at a current density of 0.1 mA cm^{-2} and an areal capacity of 0.1 mAh cm^{-2}.

confirms interfacial stability (Figure S23), revealing the stability of the HAIBSL layer during the cycling process. This improved morphology suggests that the HAIBSL facilitates the desolvation kinetics of solvated Al^{3+}, thereby promoting uniform Al plating.

Motivated by its superior performance in symmetric cells, the HAIBSL@Al electrode was therefore integrated into full cells to assess its practical viability. For this purpose, potassium cobalt hexacyanoferrate (II) ($K_2CoFe(CN)_6$) was selected as the cathode material for initial pairing investigations due to its well-defined framework and high theoretical capacity as a Prussian blue analogue (PBA). It was synthesized via a co-precipitation method following a previously reported procedure [49]. CV measurements were conducted to evaluate the redox activity of HAIBSL@Al//$K_2CoFe(CN)_6$ and bare Al//$K_2CoFe(CN)_6$ cells (Figure 5A). While the oxidation peak positions show negligible shifts, the reduction peak potential increases by approximately 0.1 V, from about 0.8 V for bare Al//$K_2CoFe(CN)_6$ to around 0.9 V for HAIBSL@Al//$K_2CoFe(CN)_6$. These results indicate that the HAIBSL reduces kinetic barriers and facilitates Al^{3+} deposition during the charging process. As shown in Figure S24, the HAIBSL@Al//$K_2CoFe(CN)_6$ cell exhibits pronounced elevation in both charge and discharge voltage plateaus compared to the bare Al//$K_2CoFe(CN)_6$ cell, fully consistent with the CV results. The rate performance was evaluated at current densities ranging from 0.1 to 0.5 A g^{-1} (Figure 5B). Although the bare Al//$K_2CoFe(CN)_6$ cell delivers an initial capacity of 48.9 mAh g^{-1}, its performance degrades sharply with increasing current densities, failing markedly at current densities higher than 0.3 mA g^{-1} due to the sluggish kinetics of the passivated Al. In contrast, the HAIBSL@Al//$K_2CoFe(CN)_6$ cell exhibits a specific capacity of approximately 78.5 mAh g^{-1} after 5 cycles at 0.1 A g^{-1} and retains 45.0 mAh g^{-1} even at 0.5 A g^{-1}. When the current density is returned to 0.1 A g^{-1}, the capacity recovers to 61.3 mAh g^{-1}, demonstrating excellent reversibility and superior rate performance, which is attributed primarily to the HAIBSL for its facilitation of rapid Al^{3+} desolvation and transport kinetics. Furthermore, the HAIBSL@Al full cell exhibits excellent long-term cycling stability (Figure 5C), retaining 52.83% of its initial activated capacity of 63.6 mAh g^{-1} after 700 cycles. This

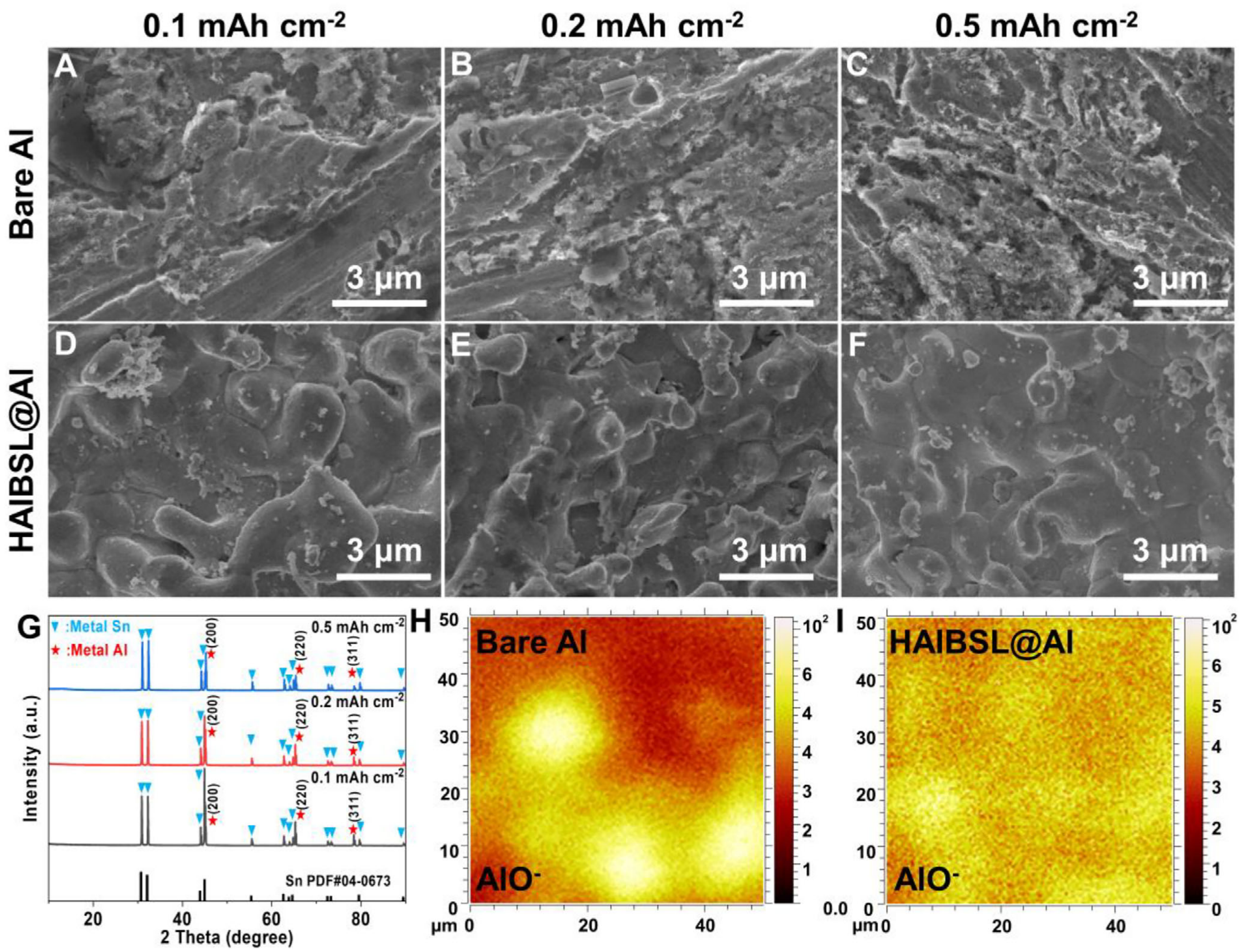

FIGURE 4 | SEM images of Al deposition with a capacity of 0.1, 0.2, and 0.5 mAh cm^{-2} at a current density of 0.05 mA cm^{-2} on bare Al (A–C), HAIBSL@Al (D-F). (G) XRD patterns of HAIBSL@Al anodes with different plating areal capacities. 2D spatial distribution of AlO^- species on the Al anode after 10 cycles: (H) bare Al and (I) HAIBSL@Al electrodes via TOF-SIMS.

contrasts sharply with the bare Al//$K_2CoFe(CN)_6$ cell, which fails abruptly after 38 cycles, due to Al passivation induced by the sluggish desolvation kinetics of hydrated Al^{3+}. The versatility of the HAIBSL@Al anode was further demonstrated using an α-MnO_2 cathode to assemble a full cell, where the α-MnO_2 was synthesized following previous literature (Figures S25 and S26) [50]. EIS reveals significantly improved interfacial kinetics in HAIBSL@Al//α-MnO_2 cell, as evidenced by a substantially lower charge-transfer resistance (200 Ω) compared to that of the bare Al//α-MnO_2 (4000 Ω) (Figure 5D). This reduction indicates that the HAIBSL effectively promotes the desolvation of hydrated Al^{3+} and enhances Al^{3+} transport. Furthermore, CV was performed at 0.05 mV s^{-1} between 0.1 and 2.0 V to evaluate the redox activity of HAIBSL@Al//α-MnO_2 and bare Al//α-MnO_2 cells (Figure 5E). In the bare Al//α-MnO_2 cell, a distinct HER peak is observed at low potentials, while the proton deintercalation process occurs at 0.35 V [51]. In contrast, the HAIBSL@Al//α-MnO_2 full cell exhibits not only lower polarization but also a smaller voltage gap between the anodic and cathodic peaks, reflecting its enhanced redox reaction kinetics. Figure S27 presents the galvanostatic charge–discharge profiles at 0.1 A g^{-1}. The bare Al//α-MnO_2 cell exhibits severe voltage polarization with a discharge plateau around 1.0 V, a characteristic behavior of reported AAMBs using bare Al anodes that undergo surface passivation. In contrast, the HAIBSL@Al//α-MnO_2 cell delivers a significantly higher discharge plateau at ≈1.3 V and a lower charge plateau at ≈1.6 V, resulting in a narrowed polarization gap of only 0.3 V, which is much smaller than that of the bare Al//α-MnO_2 cell (0.7 V). After activation, the HAIBSL@Al//α-MnO_2 cell achieves a specific capacity of 143.0 mAh g^{-1} and retains 81.5 mAh g^{-1} over 150 cycles, highlighting its stable cycling performance (Figure 5F). By comparison, the bare Al//α-MnO_2 cell delivers only 47.8 mAh g^{-1} and fails after 34 cycles, which is attributed to sluggish desolvation kinetics.

3 | Conclusion

In summary, this work designs a highly aluminophilic and ion-buffering synergistic layer on the Al anode via a facile one-step chemical displacement route. The resulting gradient composite layer, exemplified by HAIBSL composed of Sn/SnO_x, not only acts as a physical barrier against water but also effectively promotes Al^{3+} dissociation from $[Al(H_2O)_6]^{3+}$ clusters and

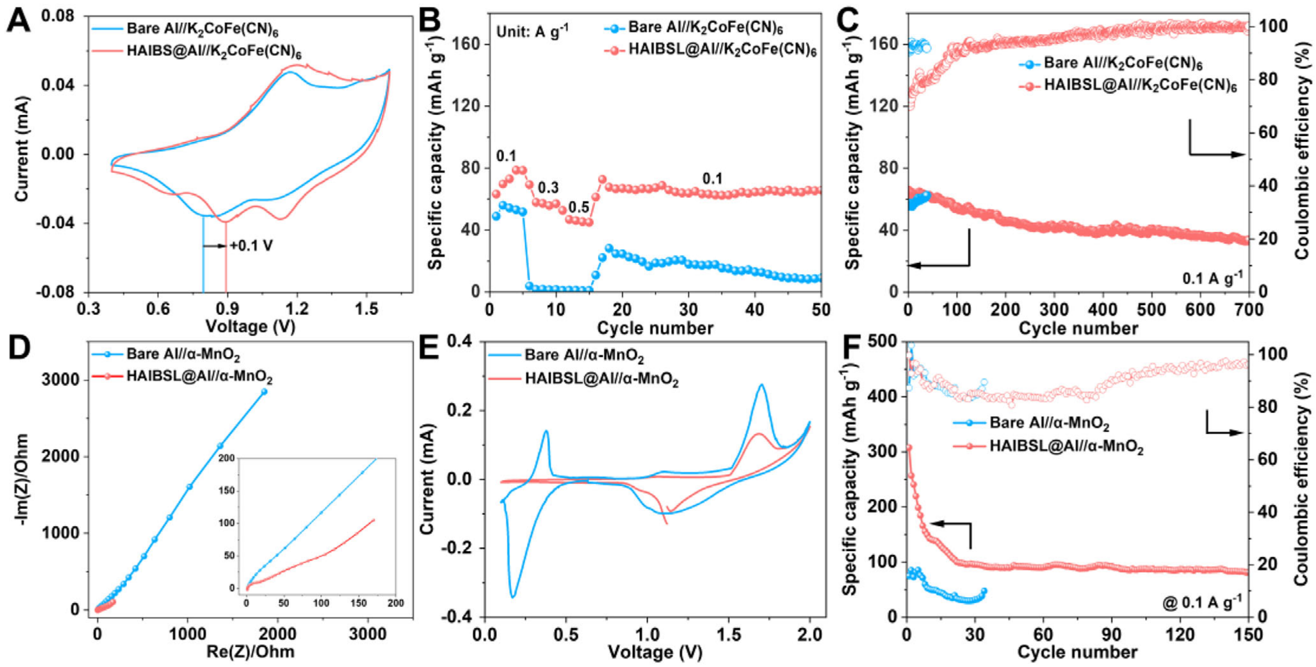

FIGURE 5 | Electrochemical properties of full cells. (A) CV curves of HAIBSL@Al//$K_2CoFe(CN)_6$ and bare Al//$K_2CoFe(CN)_6$ full cells at a scan rate of 0.1 mV s^{-1}. (B) Rate performance comparison of HAIBSL@Al//$K_2CoFe(CN)_6$ and bare Al//$K_2CoFe(CN)_6$ full cells under various current densities. (C) Cycling performance of the HAIBSL@Al//$K_2CoFe(CN)_6$ and bare Al//$K_2CoFe(CN)_6$ full cells at a current density of 0.1 A g^{-1}. (D) Nyquist plots of bare Al//α-MnO_2 and HAIBSL@Al//α-MnO_2 cells. (E) CV curves of the HAIBSL@Al//α-MnO_2 and bare Al//α-MnO_2 full cells at a scan rate of 0.05 mV s^{-1}. (F) Cycling performance of bare Al//α-MnO_2 and HAIBSL@Al//α-MnO_2 cells at a specific current of 0.1 A g^{-1}.

guides homogeneous lateral Al^{3+} transport. These dual functions accelerate desolvation kinetics while concurrently suppressing water-induced side reactions and dendritic growth. Electron microscopy, Raman spectroscopy, and theoretical simulations collectively corroborate that the high aluminophilicity and ion-buffering capability of the HAIBSL layer enable highly uniform Al deposition. As a result, the HAIBSL@Al symmetric cell exhibits remarkable stability, operating steadily for over 1800 h at 0.05 mA cm^{-2}. In full-cell configurations with representative cathodes ($K_2CoFe(CN)_6$ and α-MnO_2), the HAIBSL@Al anode also delivers exceptional cycling performance, retaining 52.83% capacity after 700 cycles compared to only 38 cycles for the bare Al//$K_2CoFe(CN)_6$ cell, and sustaining 81.5 mAh g^{-1} after 150 cycles compared to 47.8 mAh g^{-1} (failure at 34 cycles) for bare Al//α-MnO_2 cell. Together, these results validate the effectiveness of the HAIBSL design and establish it as a high-performance interfacial strategy for developing stable metal anodes.

Acknowledgements

Dr. Jian Wang thanks the fellowship supported by the Alexander von Humbolt Foundation. The authors acknowledge the National Key R&D Program of China (2021YFA1201503), Natural Science Foundation of China (Nos. 22279161, 22572217 and 22309144), China Postdoctoral Science Foundation (No. 2024M762318), Jiangsu Provincial Science and Technology Program (Grant: BG 2024020), Open Project of Inner Mongolia Engineering Research Center of Lithium-Sulfur Battery Energy Storage (No. MDK2025071), Opening funding from Key Laboratory of Engineering Dielectrics and Its Application (No. KFM202507, Ministry of Education) as well as Guangdong Basic and Applied Basic Research Foundation (2024A1515110244). Dr. Wang thanks the support from the Tongling University Talent Program under Grant No. 2023tlxyrc44, and the Tongling University Natural Science Research Project under Grant No. 2024tlxykjZD05. The authors also thank the scientific-technical support from Nano-X in the Suzhou Institute of Nano-tech and Nano-bionics, China Academy of Sciences.

Open access funding enabled and organized by Projekt DEAL.

Conflicts of Interest

The authors declare no conflicts of interest.

Data Availability Statement

The data that support the findings of this study are available from the corresponding author upon reasonable request.

References

1. J. Yu, D. Wang, D. Zhao, W. Zhang, and Q. Zhu, “Challenges and Strategies for Constructing Stable Aluminum Metal Anodes in Rechargeable Aluminum-Ion Batteries,” *Materials Today* 88 (2025): 888–905.

2. Y. Zhang, Y. Ge, H. Xu, et al., “Design Principles of Underpotential Deposition Chemistry for Highly Reversible Multivalent Metal Anodes,” *Energy Storage Materials* 74 (2025): 103991.

3. S. Chen, N. A. Gadelhak, Y. Wu, et al., “Aqueous Aluminium-Ion Batteries: Cathode Material Design, Anode Engineering and Electrolyte Innovation,” *Small* 22 (2025): 07888.

4. J. Zhang, R. He, L. Jia, et al., “Strategies for Realizing Rechargeable High Volumetric Energy Density Conversion-Based Aluminum–Sulfur Batteries,” *Advanced Functional Materials* 33 (2023): 2305674.

5. Q. Hao, F. Chen, X. Chen, Q. Meng, Y. Qi, and N. Li, “Highly Stable Al Metal Anode Enabled by Surface Chemical Passivation for Long-Life

Aqueous Al Metal Batteries," *ACS Applied Materials & Interfaces* 15 (2023): 34303–34310.

6. Q. Hao, F. Chen, X. Chen, Q. Meng, Y. Qi, and N. Li, "Bi-Functional Poly(vinylidene difluoride) Coated Al Anodes for Highly Rechargeable Aqueous Al-Ion Batteries," *Electrochimica Acta* 421 (2022): 140495.

7. R. Xiao, J. Chen, K. Fu, et al., "Hydrolysis Batteries: Generating Electrical Energy during Hydrogen Absorption," *Angewandte Chemie International Edition* 57 (2018): 2219–2223.

8. K. Bhimani, A. Anjan, V. Mahajani, R. M. Manoj, and N. Koratkar, "Tuning the Aluminum–Water Interface in Aqueous Aluminum Metal Batteries," *ACS Applied Energy Materials* 8 (2025): 6194–6202.

9. H. Cheng, Y. Lu, Z. Li, et al., "Nuclear Quantum Confinement Enables Robust Deuterium Bonds for Highly Reversible Aluminum Anodes," *Angewandte Chemie International Edition* 64 (2025): 202508422.

10. Y. Liu, E. Hu, B. Yang, et al., "Solvation-Structure Design of Multicomponent Eutectic Electrolytes Enabling Al-Rich Alloy Growth in Aqueous Aluminum-Ion Batteries," *Journal of the American Chemical Society* 148 (2026): 1220–1232.

11. D. Y. Wang, E. Hu, G. Wu, et al., "Chelation-Driven Electrolyte Design for Enhanced Interface and Electrochemical Window in Aqueous Aluminum Batteries," *Angewandte Chemie International Edition* 64 (2025): 202508641.

12. Q. Dou, N. Yao, W. K. Pang, et al., "Unveiling Solvation Structure and Desolvation Dynamics of Hybrid Electrolytes for Ultralong Cyclability and Facile Kinetics of Zn–Al Alloy Anodes," *Energy & Environmental Science* 15 (2022): 4572–4583.

13. D. Chen, X. Ma, W. Xu, et al., "Disrupting Hydrogen Bond Network Connectivity with a Double-Site Additive for Long-Life Aqueous Zinc Metal Batteries," *Exploration* 5 (2025): 20240007.

14. A. Zhou, L. Jiang, J. Yue, et al., "Water-in-Salt Electrolyte Promotes High-Capacity FeFe(CN)$_6$ Cathode for Aqueous Al-Ion Battery," *ACS Applied Materials & Interfaces* 11 (2019): 41356–41362.

15. Y. Gao, Y. Li, H. Yang, L. Zheng, Y. Bai, and C. Wu, "Bi-Salt Electrolyte for Aqueous Rechargeable Aluminum Battery," *Journal of Energy Chemistry* 67 (2022): 613–620.

16. D. Dong, C.-X. Zhao, X. Zhang, and C. Wang, "Aqueous Electrolytes: From Salt in Water to Water in Salt and beyond," *Advanced Materials* 37 (2025): 2418700.

17. O. Borodin, J. Self, K. A. Persson, C. Wang, and K. Xu, "Uncharted Waters: Super-Concentrated Electrolytes," *Joule* 4 (2020): 69–100.

18. Z. Zhao, Z. Zhang, W. Wang, T. Xu, and X. Yu, "Strengthen Water O−H Bond in Electrolytes for Enhanced Reversibility and Safety in Aqueous Aluminum Ion Batteries," *Angewandte Chemie International Edition* 64 (2025): 202415436.

19. Z. Yang, P. Meng, M. Jiang, et al., "Realizing Rechargeable Cathode-Free Aluminum-Ion Batteries via Regulating Solvation Structure in Aqueous-Aprotic Electrolytes," *Journal of Energy Chemistry* 99 (2024): 466–474.

20. Z. Zhao, Z. Zhang, T. Xu, W. Wang, B. Wang, and X. Yu, "Solvation Structure Regulation for Highly Reversible Aqueous Al Metal Batteries," *Journal of the American Chemical Society* 146 (2024): 2257–2266.

21. X. Xu, Q. Pang, X. Liu, et al., "A Long-Lifespan Prussian Blue-Based Aluminum Metal Battery Using an Aqueous/Organic Hybrid Electrolyte," *Electrochimica Acta* 512 (2025): 145503.

22. P. Meng, J. Huang, Z. Yang, et al., "Air-Stable Binary Hydrated Eutectic Electrolytes with Unique Solvation Structure for Rechargeable Aluminum-Ion Batteries," *Nano-Micro Letters* 15 (2023): 188.

23. G. R. Pastel, Y. Chen, T. P. Pollard, et al., "A Sobering Examination of the Feasibility of Aqueous Aluminum Batteries," *Energy & Environmental Science* 15 (2022): 2460–2469.

24. W. Chu, X. Zhang, S. Zhao, et al., "High-Voltage Deep Eutectic Solvent Electrolyte with Fluorine-Substituted Acetamide Additive for Aluminum-Ion Battery," *Advanced Functional Materials* 34 (2024): 2305194.

25. H. Lv, S. Yang, C. Li, et al., "Suppressing Passivation Layer of Al Anode in Aqueous Electrolytes by Complexation of H_2PO_4- to Al^{3+} and an Electrochromic Al Ion Battery," *Energy Storage Materials* 39 (2021): 412–418.

26. J. Dong, X. Cheng, H. Yang, et al., "Suspension Electrolytes with Catalytically Self-Expediating Desolvation Kinetics for Low-Temperature Zinc Metal Batteries," *Advanced Materials* 37 (2025): 2501079.

27. C. Yan, C. Lv, B. Jia, et al., "Reversible Al Metal Anodes Enabled by Amorphization for Aqueous Aluminum Batteries," *Journal of the American Chemical Society* 144 (2022): 11444–11455.

28. H. Yu, X. Zhang, Y. Wang, et al., "Activation and Stabilization Strategies of Aluminum Metal Anode toward High Performance Aqueous Al Metal Batteries," *Advanced Materials* 37 (2025): 2507164.

29. H. Yu, C. Lv, C. Yan, and G. Yu, "Interface Engineering for Aqueous Aluminum Metal Batteries: Current Progresses and Future Prospects," *Small Methods* 8 (2024): 2300758.

30. J. Wang, J. Zhang, Y. Zhang, et al., "Atom-Level Tandem Catalysis in Lithium Metal Batteries," *Advanced Materials* 36 (2024): 2402792.

31. J. Wang, J. Zhang, X. Cheng, et al., "Electrode/Electrolyte Interface Studies of Rechargeable Li Batteries with Interface-Specific Sum Frequency Generation Spectroscopy," *Journal of the American Chemical Society* 147 (2025): 44633–44651.

32. J. Wang, J. Zhang, J. Wu, et al., "Interfacial "Single-Atom-in-Defects" Catalysts Accelerating Li^+ Desolvation Kinetics for Long-Lifespan Lithium-Metal Batteries," *Advanced Materials* 35 (2023): 2302828.

33. F. Zhu, J. Wang, Y. Zhang, et al., "Low-Temperature Lithium Metal Batteries Achieved by Synergistically Enhanced Screening Li^+ Desolvation Kinetics," *Advanced Materials* 37 (2025): 2411601.

34. J. Zhang, F. Liu, R. He, et al., "Taming Interfacial Ion-Dipole Interactions with d -Orbital Delocalized Electron Catalysis Expediates Low-Temperature Li Metal Batteries," *Advanced Materials* 38 (2026): 10894.

35. Q. Zhao, M. J. Zachman, W. I. Al Sadat, J. Zheng, L. F. Kourkoutis, and L. Archer, "Solid Electrolyte Interphases for High-Energy Aqueous Aluminum Electrochemical Cells," *Science Advances* 4 (2018): aau8131.

36. C. Li, Z. Lv, H. Du, et al., "Optimization of an Artificial Solid Electrolyte Interphase Formed on an Aluminum Anode and Its Application in Rechargeable Aqueous Aluminum Batteries," *ACS Applied Materials & Interfaces* 15 (2023): 50166–50173.

37. Q. Sun, Y. Pang, H. Pan, W. Zhang, and Z. Li, "Constructing an Artificial SEI Layer Rich-AlF3 Based on Molecular Scale in Aqueous Aluminum Batteries to Avoid Anode Passivation and Hydrogen Evolution Reactions," *Chemical Engineering Journal* 489 (2024): 151296.

38. E. Hu, B. E. Jia, W. Nong, et al., "Boosting Aluminum Adsorption and Deposition on Single-Atom Catalysts in Aqueous Aluminum-Ion Battery," *Advanced Energy Materials* 14 (2024): 2401598.

39. B. Jia, E. Hu, Z. Hu, et al., "Laminated Tin–aluminum Anodes to Build Practical Aqueous Aluminum Batteries," *Energy Storage Materials* 65 (2024): 103141.

40. Q. Ran, H. Shi, H. Meng, et al., "Aluminum-Copper Alloy Anode Materials for High-Energy Aqueous Aluminum Batteries," *Nature Communications* 13 (2022): 576.

41. Q. Ran, S. P. Zeng, M. H. Zhu, et al., "Uniformly MXene-Grafted Eutectic Aluminum-Cerium Alloys as Flexible and Reversible Anode Materials for Rechargeable Aluminum-Ion Battery," *Advanced Functional Materials* 33 (2022): 2211271.

42. S. Li, X. Li, C. Dai, W. He, Y. Shabdan, and M. Guli, "Research on the Application of Metal Oxide Buffer Layers in Perovskite Solar Cells," *Chemical Engineering Journal* 521 (2025): 166935.

43. S. Li, J. Fu, G. Miao, et al., "Toward Planar and Dendrite-Free Zn Electrodepositions by Regulating Sn-Crystal Textured Surface," *Advanced Materials* 33 (2021): 2008424.

44. J. Zhang, L. Pan, L. Jia, et al., "Delocalized Electron Engineering of MXene-Immobilized Atomic Catalysts toward Fast Desolvation and Dendritic Inhibition for Low-Temperature Zn Metal Batteries," *Nano Letters* 25 (2025): 3756–3765.

45. H. Yang, F. Liu, B. Chen, et al., "Edge-Electron Induced Ferrimagnetic Effect to Accelerate Interfacial Desolvation Kinetics toward Dendrite-Free Zn Metal Batteries," *Chemical Engineering Journal* 519 (2025): 164989.

46. W. Wang, J. Dong, H. Hu, et al., "Gradient Desolvation–Diffusion Kinetic Layer Promoters for Low-Temperature Dendrite-Free Zn Metal Batteries," *Nano Letters* 25 (2025): 10376–10385.

47. Y. Fu, J. You, Q. Yao, et al., "Modulating Solvation Structure and Desolvation Dynamics of Hydrate Eutectic Electrolytes for Cost-Effectiveness, Ultralong Cyclability, and High Reversibility of Zn–Al Alloy Anode," *ACS Sustainable Chemistry & Engineering* 13 (2025): 19658–19667.

48. X. Cheng, W. Wang, Z. Tang, et al., "Expediting Desolvation–Diffusion Kinetics by Self-Cascade Catalysis for Durable Low-Temperature Zinc Metal Batteries," *Angewandte Chemie International Edition* 65 (2026): 22417.

49. Y. Ru, S. Zheng, H. Xue, and H. Pang, "Potassium Cobalt Hexacyanoferrate Nanocubic Assemblies for High-Performance Aqueous Aluminum Ion Batteries," *Chemical Engineering Journal* 382 (2020): 122853.

50. X. Yang, Q. Sun, L. Chai, et al., "α-MnO_2 Cathode with Oxygen Vacancies Accelerated Affinity Electrolyte for Dual-Ion Co-Encapsulated Aqueous Aluminum Ion Batteries," *Small* 20 (2024): 2400335.

51. H. Ze, X. Fan, Z. Yang, et al., "Deciphering the Competitive Charge Storage Chemistry of Metal Cations and Protons in Aqueous MnO_2 -Based Supercapacitors," *Journal of the American Chemical Society* 147 (2025): 9620–9628.

Supporting Information

Additional supporting information can be found online in the Supporting Information section.

Supporting File: adfm76179-sup-0001-SuppMat.docx.